Measurements of Chromospheric Mg I Emission Lines of Zero-Age Main-Sequence Stars

Mai Yamashita[1], **Yoichi Itoh**[1]

[1]Nishi-Harima Astronomical Observatory, Center for Astronomy, University of Hyogo, 407-2 Nishigaichi, Sayo, Sayo, Hyogo 679-5313

*E-mail: yamashita@nhao.jp

Received ⟨2021 November 16⟩; Accepted ⟨2021 February 4⟩

Abstract

The chromosphere is the active atmosphere in which energetic eruption events, such as flares, occur. Chromospheric activity is driven by the magnetic field generated by stellar rotation and convection. The relationship between chromospheric activity and the Rossby number, the ratio of the rotational period to the convective turnover time, has been extensively examined for many types of stars, by using narrow chromospheric emission lines, such as the Ca II lines and the Mg II h and k lines. However, the stars with small Rossby numbers, i.e., stars with rapid rotations and/or long convective turnover times, show constant strengths of such lines against the Rossby number. In this study, we investigate the infrared Mg I emission lines at $8807\,\text{Å}$ of 47 zero-age main-sequence (ZAMS) stars in IC 2391 and IC 2602 using the archive data of the Anglo-Australian Telescope at the University College London Echelle Spectrograph. After subtracting the photospheric absorption component, the Mg I line is detected as an emission line for 45 ZAMS stars, whose equivalent widths are between $0.02\,\text{Å}$ and $0.52\,\text{Å}$. A total of 42 ZAMS stars show the narrower Mg I emission lines instead of the Ca II infrared triplet emission lines, suggesting that they are formed at different depths. The ZAMS stars with smaller Rossby numbers show stronger Mg I emission lines. The Mg I emission line is not saturated even in "the saturated regime of the Ca II emission lines," i.e., Rossby number $< 10^{-1.1}$. The Mg I emission line is considered to be a good indicator of chromospheric activity, particularly for active objects.

Key words: stars: chromospheres — stars: activity — techniques: spectroscopic

1 Introduction

The chromosphere is the active atmosphere in which flares and other energetic eruption phenomena occur. It is claimed that chromospheric activity is driven by the magnetic fields induced by the dynamo process. In the dynamo process, the Coriolis force (= rotational moment $\times$ convection velocity) balances the Lorentz force (= current $\times$ magnetic strength / density of plasma) (Baliunas et al. 1996). Stellar rotation and convection are considered to be the main processes that drive the evolution of magnetic activities. Noyes et al. (1984) used the Rossby number, $N_{\rm R}$, as an indicator of stellar activity. It is defined as $P/\tau_{\rm c}$, where P is the stellar rotational period and $\tau_{\rm c}$ is the convective turnover time. $N_{\rm R}$ can be approximated as the inverse square of the dynamo number, N_D, the wave solution of the dynamo equation. Magnetic fields develop when $|N_D| > 1$.

The relationship between chromospheric line strength and the Rossby number has been extensively examined for main-sequence stars. Skumanich et al. (1972) found that the luminosity of the Ca II emission lines and rotational velocity of a solar-type star with an age of $10^8\,{\rm yr}$ are one order of magnitude larger than those of stars with an age of $10^{10}\,{\rm yr}$. Linsky, Hunten & Sowell (1979) obtained profiles of the Ca II infrared triplet (IRT) line at $\lambda 8542\,{\rm \AA}$ in 49 main-sequence or giant stars of spectra type F9-K3. For active chromospheric stars, they found that the line cores are filled in compared to quiet chromospheric stars of the same spectral type. They claimed that a better way of testing for chromospheric emission on the photospheric absorptinon is to subtract the profiles of similar spectral type stars. As a result, they showed strong evidence of chromospheric emissoin component beyond the line core for active stars. Soderblom et al. (1993) revealed strong Ca II IRT ($\lambda 8498, 8542, 8662\,{\rm \AA}$) emission lines of low-mass stars in a young open cluster M45. Marsden et al. (2009) also detected Ca II IRT emission lines of low-mass stars in young open clusters IC 2391 and IC 2602. The cluster members are considered to be on the zero-age main-sequence (ZAMS) or in the last evolution phase to the ZAMS. Soderblom et al. (1993) and Marsden et al. (2009) calculated $R'_{\rm IRT}$ from the equivalent widths (EQWs). $R'_{\rm IRT}$ describes the ratio of the surface flux of the Ca II IRT emission lines to the stellar bolometric luminosity. They found that for stars with $N_{\rm R} \geq 10^{-1.1}$, $R'_{\rm IRT}$ decreases with increasing $N_{\rm R}$. This region is called the unsaturated regime. In contrast, $R'_{\rm IRT}$ is constant at levels of approximately $10^{-4.2}$ for stars with $N_{\rm R} \leq 10^{-1.1}$. This region is called the saturated regime. Marsden

et al. (2009) suggested that the chromosphere is completely filled by the emitting regions for the stars in the saturated regime.

Yamashita et al. (2020) investigated the relation between $N_{\rm R}$ and the Ca II IRT emission lines of 60 pre-main sequence (PMS) stars. Only three PMS stars showed broad and strong emissions, indicative of large mass accretion. Most of the PMS stars present narrow and weak emissions, suggesting that their emission lines are formed in the chromosphere. All their Ca II IRT emission lines have $R'_{\rm IRT} \sim 10^{-4.2}$, which is as large as the maximum $R'_{\rm IRT}$ of ZAMS stars. The PMS stars show $N_{\rm R} < 10^{-0.8}$ and constant $R'_{\rm IRT}$ against $N_{\rm R}$, i.e., their Ca II IRT emission lines are saturated.

In this study, we examined the infrared Mg I emission line at $\lambda 8807\,\text{Å}$ (3d–3p transition) as a representative unsaturated chromospheric emission line. This Mg I emission line was isolated from other strong absorption lines. It was detected with numerous chromospheric emission lines during a total solar eclipse in 1962 (Dunn et al. 1968). The solar imaging with the infrared Mg I emission line suggested that the emission line is formed in the chromosphere $500\,\text{km}$ above the photosphere (Fleck et al. 1994). As other example, the prominent infrared Mg I emission line was detected from eight T Tauri stars.

Specifically, we investigated the infrared Mg I emission lines of 47 ZAMS stars using high-resolution spectral data. We examined the relationship between the Rossby number and the Mg I emission line strength. In the next section, we describe the observations and the data reduction procedure. In Section 3, we present the results, and in Section 4, we discuss the origin of the Mg I emission line and the correlation of the line strength and the Rossby number.

2 Observations and Data Reduction

2.1 Stellar parameters

Our targets are F, K, and G-type ZAMS stars in IC 2391 ($50 \pm 5\,\text{Myr}$; Barrado y Navascues et al. 2004) and IC 2602 ($30 \pm 5\,\text{Myr}$; Stauffer et al. 1997). The metallicity of both clusters has been determined to be close to the Sun, which is $[\text{Fe/H}] = -0.01 \pm 0.02$ for IC 2391 (D'Orazi & Randich 2009) and $[\text{Fe/H}] = 0.00 \pm 0.01$ for IC 2602 (Randich et al. 2001).

A total of 52 ZAMS stars are confirmed as single stars in the IC 2391 and IC 2602 members based on the strength of the lithium $6708\,\text{Å}$ absorption line (Marsden et al. 2009). We examined the proper motion and radial velocity of these stars. The proper motion and the radial velocity are referred from *Gaia* Data Release 2 (DR2) (Gaia Collaboration 2018). For IC 2391, the mean proper motion in RA and Dec are $-23.6 \pm 4.7\,\text{km}\cdot\text{s}^{-1}$ and $22.0 \pm 4.4\,\text{km}\cdot\text{s}^{-1}$, respectively. For IC 2602, the corresponding values are $-17.3 \pm 1.0\,\text{km}\cdot\text{s}^{-1}$ and $10.8 \pm 1.3\,\text{km}\cdot\text{s}^{-1}$. Based on the observations

in *Gaia* DR2 (Soubiran et al. 2018), for 51 objects in IC 2391 and 325 objects in IC 2602, Gutierrez Albarran et al. (2020) obtained mean radial velocities of $14.9 \pm 0.6\,\mathrm{km \cdot s^{-1}}$ and $17.8 \pm 0.7\,\mathrm{km \cdot s^{-1}}$, respectively. VXR PSPC 02A, VXR PSPC 31, VXR PSPC 78, and [RSP95] 96 have both proper motion and radial velocity that deviated by more than 3σ from the mean values. [RSP95] 42C has both proper motion and parallax that deviated by more than 3σ from the mean values. They were removed from our target list. A total of 47 targets were investigated in this study, which are presented in Table 1.

2.2 Data Reduction

2.2.1 Photometry

To obtain the rotational period, P, we analyzed the light curves of 39 ZAMS stars. The members of IC 2391 and IC 2602 were observed in Transiting Exoplanet Survey Satellite (*TESS*) Sectors 8 and 10, respectively. All 39 stars were observed in the long-cadence (1800-second exposure) mode, which continued for $27\,\mathrm{days}$. These data were retrieved from the Multimission Archive at the Space Telescope Science Institute. We conducted principal component analysis using eleanor, an open-source tool for extracting light curves from *TESS* full-frame images (Feinstein et al. 2019). After the photometric measurements, we searched for periodic signals by conducting Lomb–Scargle (Scargle 1982) periodogram analysis. For each object, the period of the light curve was determined. VXR PSPC 44 presented beating signatures in its light curve; therefore, we adopted the second maximum of the power. We calculated the amplitudes of the light curves by taking the 90th percentile flux and subtracting it from the 10th percentile flux. For three objects having $\mathrm{amplitude/mean\,flux\,error} < 10$ (Cl* IC2391 L32, VXR PSPC 7, and [RSP95] 7), we referred the periods listed in Marsden et al. (2009). We used the periods or $v \sin i$ listed in Marsden et al. (2009) for three objects not observed by the *TESS*. The derived periods are listed in Table 1. They show good correlation with the periods measured by Patten & Simon (1996) and Barnes et al. (1999), with a correlation coefficient of 0.997.

2.2.2 Spectroscopy

We investigated the Mg I line, Hα line, and Ca II IRT lines of the considered 47 ZAMS stars using the $3.9\,\mathrm{m}$ Anglo-Australian Telescope (AAT) and the University College London Echelle Spectrograph (UCLES) archived spectra. The principal investigator was S. C. Marsden. The dates of the observations were March 17–19, 2000; January 6–8, 2001; and February 11–12, 2001. The wavelength coverage was between $3522\,\mathrm{Å}$ and $9386\,\mathrm{Å}$ ($R \equiv \frac{\lambda}{\Delta\lambda} \sim 40,000 - 120,000$). The integration time for each object was between $300\,\mathrm{s}$ and $1200\,\mathrm{s}$. The number of frames obtained for each ZAMS star ranged from two to six. A detailed description of the observations is presented in Marsden et al. (2009).

We used the Image Reduction and Analysis Facility (IRAF) software package[1] for data reduction. Overscan subtraction, bias subtraction, flat fielding, removal of scattered light, removal of cosmic rays and OH airgrow, extraction of a spectrum, wavelength calibration using a Tr–Ar lamp, and continuum normalization were conducted for all UCLES spectra. After the wavelength calibration, only 12 orders (order $64-67, 75-76, 84-87$, and $94-95$) were reduced.

To improve the S/N ratio, we combined and averaged multiple frames for each object. Moreover, the UCLES spectrum overlaps with the next order over several tens of Angstroms. The average ratio of the intensity to the next order was 1.8, which was independent of the wavelength. We applied a weight of 1.8 to each short spectrum.

We subtracted the photospheric absorption component for all spectra. The Mg I emission component is typically buried by the photospheric absorption, as shown in Figure 1. Inactive stars with a spectral type similar to that of the target were used as template stars. We reduced the UCLES spectra of HD 16673 (F6V), α Cen A (G2V), and α Cen B (K1V). We also obtained the VLT archive spectra of ten inactive stars chosen from the inactive stars library (Yee, Petigura & von Braun 2017) and the UVES POP library: ζ Ser (F2IV), HD 3861 (F8V), HD 1388 (G0V), HD 156846 (G1V), HD 109749 (G3V), HIP 94256 (G5V), HD 190360 (G7V), HD 217107 (G8V), HD 16160 (K3V), and HD 165341B (K4V). According to Yee, Petigura & von Braun (2017) and Nordstom et al. (2004), their metallicity is $-0.11 \leq [\mathrm{Fe/H}] \leq 0.31$. Their surface gravity is $4.01 \leq \log \mathrm{g} \leq 4.64\,\mathrm{cm \cdot s^{-2}}$. The differences in the surface gravities of the target and template stars were sufficiently small, and therefore, were not expected to change the strengths of the photospheric absorption lines. For each template star, we reduced several frames, followed by averaging. The spectrum of an inactive star was shifted to match the radial velocity of the target star. For correcting the rotational broadening, the spectra of the template stars were convolved with a Gaussian kernel to match the widths of the absorption lines of each target. Using the high-S/N spectra of the inactive stars, we carefully subtracted the photospheric absorption component. We considered the photospheric subtraction to be reliable if the photospheric absorption lines did not show any emission or absorption component. Many Fe I absorption lines appeared in the spectra of the targets and templates. However, the emission components of Fe I may be formed in a lower chromosphere (Vernazza et al. 1981). Actually, T Tauri stars show narrow Fe I and Fe II emission lines at rest velocity, which are believed to be formed in the chromosphere (Hamann & Persson 1992). In contrast, we used Ni I ($6644, 6728, 7525\,\mathrm{\AA}$), Mn I ($6014, 6017, 6022\,\mathrm{\AA}$), V I ($6039\,\mathrm{\AA}$), and Ti I ($7523\,\mathrm{\AA}$) as the photospheric absorption lines. These absorption lines were isolated and relatively deep. We measured the standard deviation of the counts at

[1] IRAF software is distributed by the National Optical Astronomy Observatories, which are operated by the Association of Universities for Research in Astronomy, Inc., under a cooperative agreement with the National Science Foundation.

Ni I ($\lambda 6644\,\text{Å}$) after the subtraction of the spectrum of the inactive star, $\sigma_{\text{Ni I}}$. The wavelength range was set as the wing width of the Ni I absorption line before the subtraction. σ_{cont} is the standard deviation of the counts between $\lambda 6683$ and $6693\,\text{Å}$, where there was no strong feature. $\sigma_{\text{Ni I}}/\sigma_{\text{cont}} \sim 1$ represents the appropriate subtraction of the photospheric absorption. $\sigma_{\text{Ni I}}/\sigma_{\text{cont}}$ of the ZAMS stars were between 0.59 and 2.51. In principle, $\sigma_{\text{Ni I}}$ is greater than σ_{cont}, because the number of photons in the Ni I absorption line is smaller than that in the continuum. We considered that the photospheric subtraction was reliable if $\sigma_{\text{Ni I}}/\sigma_{\text{cont}} < 1.2$. A total of 30 ZAMS stars showed $\sigma_{\text{Ni I}}/\sigma_{\text{cont}} < 1.2$, and the remaining 17 ZAMS stars showed $\sigma_{\text{Ni I}}/\sigma_{\text{cont}} \geq 1.2$.

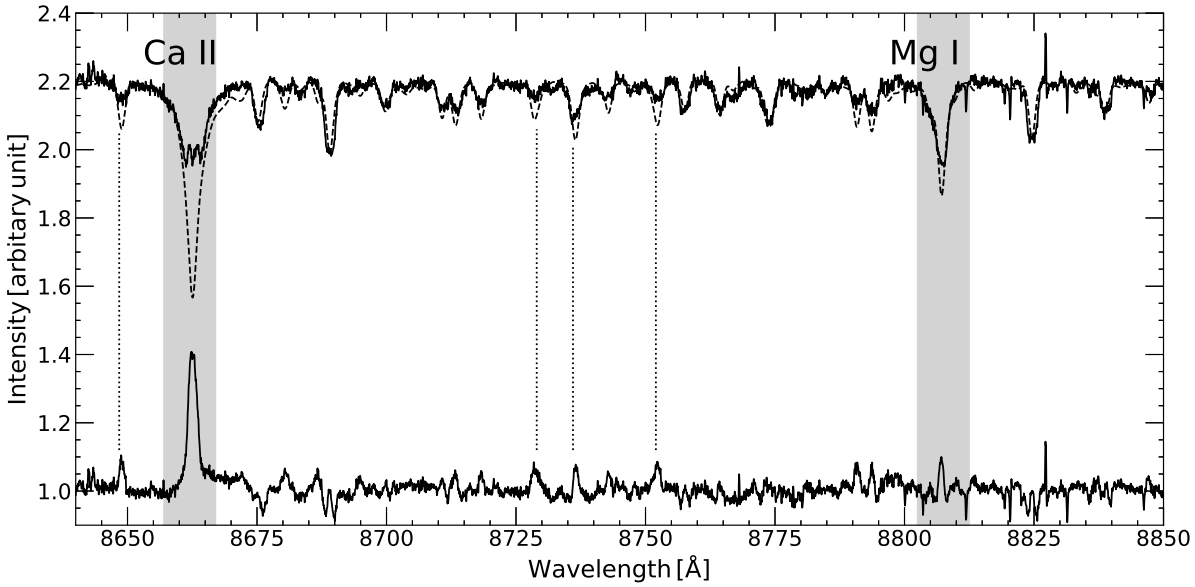

Fig. 1: Procedure of spectral subtraction of photospheric component for ZAMS star. Observed spectrum of [RSP95] 43 is shown in top part of panel with solid line. Dotted line represents spectrum of fitted inactive template star. Spectra of [RSP95] 43 and template star are shown shifted by $+1.2$ for display purposes. Difference between spectra of [RSP95] 43 and template star is shown in bottom of panel, which is shifted by $+1$. Ca II line ($\lambda 8662\,\text{Å}$) and Mg I line ($\lambda 8808\,\text{Å}$) appear in emission. Other emission lines such as Si I ($\lambda 8648, 8729, 8752\,\text{Å}$) and Mg I ($\lambda 8736\,\text{Å}$) are also detected.

Before measuring the EQWs, the continuum components of the spectra were added to unity. To obtain the EQWs of the Mg I and Hα emission lines, the areas of the corresponding emission profiles were directly integrated. The EQW errors were estimated by multiplying the standard deviation of the continuum by the wavelength range of the emission lines of each ZAMS star. We estimated the standard deviations of the continuums near the Mg I and Hα emission lines. The wavelength range was $\lambda 8798 - 8802\,\text{Å}$ and $\lambda 8813 - 8819\,\text{Å}$ for the Mg I emission line, and that for the Hα emission line was $\lambda 6615 - 6623\,\text{Å}$. In these wavelength ranges, no strong features were observed. We also measured the full width at half maximums (FWHMs) of the Mg I and Ca II IRT emission lines by

fitting with a Gaussian function. The Ca II IRT lines at $\lambda 8542\,\text{Å}$ of some template stars were out of range, and we did not measure their FWHMs.

Table 1: Physical parameters of the ZAMS stars in IC 2391 and IC 2602.

Object Name	r	i	$L/L_\odot$	$T_{\rm eff}$	$(B-V)_0$	dist	Period	$v \sin i$	M_*	$\tau_{\rm c}$
	[mag]	[mag]		[K]	[mag]	[pc]	[days]	$[\mathrm{km \cdot s^{-1}}]$	$[M_\odot]$	$\times 10^5$ [s]
(1)	(2)	(3)	(4)	(5)	(6)	(7)	(8)	(9)	(10)	(11)
IC 2391										
Cl* IC2391 L32	9.7	9.2	3.27	6590	0.43	150	-	68	1.5	1
VXR PSPC 3A	10.8	10.6	0.83	5607	0.67	150	3.93	10	1.0	15
VXR PSPC 7	9.5[a]	9.4	2.43	6472	0.45	146	-	21	1.4	2
VXR PSPC 12	11.6	11.4	0.41	5042	0.83	152	3.69	10	0.9	25
VXR PSPC 14	10.3	10.2	1.42	5768	0.56	158	1.35	43	1.1	11
VXR PSPC 16A	11.5	11.3	0.44	5093	0.87	152	-	21	0.9	25
VXR PSPC 22A	10.8	10.6	0.76	5587	0.73	148	2.31	8	1.0	15
VXR PSPC 35A	12.2	11.8	0.25	4982	0.99	150	0.26	89	0.8	25
VXR PSPC 44	9.7	9.4	2.64	6536	0.41	151	0.57	79	1.4	1
VXR PSPC 45A	10.5[a]	9.8[b]	1.19	5125	0.80	151	0.22	235	1.2	25
VXR PSPC 50A	-	11.6	0.21[b]	5210[b]	0.84	145[c]	-	56	0.8	20
VXR PSPC 52	10.2	10.1	1.48	5949	0.56	156	2.15	10	1.2	11
VXR PSPC 62A	11.6	11.3	0.45	4914	0.85	151	0.50[b]	49	0.9	25
VXR PSPC 66	9.7	9.5	2.36	6382	0.46	150	0.92	52	1.3	2
VXR PSPC 67A	11.4	11.1	0.55	5004	0.95	149	3.41	9	1.0	25
VXR PSPC 69A	11.3	11.1	0.43	5062	0.83	149	2.22	19	0.9	25
VXR PSPC 70	10.6	10.4	0.99	5737	0.63	152	2.61	16	1.0	15
VXR PSPC 72	11.3	11.1	0.54	5336	0.72	151	3.05	13	0.9	20
VXR PSPC 76A	12.4	12.0	0.22	4776	1.04	150	4.58	7	0.8	25
VXR PSPC 77A	9.9	9.6	2.14	6163	0.49	152	0.65	93	1.3	7
VXR PSPC 80A	-	11.0[b]	0.38[b]	4880[b]	0.96	145[c]	-	145	0.9	25
IC 2602										
Cl* IC2602 W79	11.3	11.1	0.48[b]	5500[b]	0.79	150	6.55	8	0.9	31
[RSP95] 1	11.3	11.0	0.56	5198	0.87	149	3.85	7	0.9	31
[RSP95] 7	9.4	9.0	3.74	6610	0.40	150	-	58	1.5	1
[RSP95] 8A	-	9.8[b]	1.27[b]	6190[b]	0.61	145[c]	-	27	1.2	7
[RSP95] 10	-	11.6[b]	0.22[b]	4520[b]	1.19	145[c]	3.16	14	0.8	42
[RSP95] 14	11.4	11.2	0.45	5071	0.83	149	2.73	11	0.9	31
[RSP95] 15A	-	10.7[b]	0.48[b]	4920[b]	0.89	145[c]	3.6[b]	7	1.0	31
[RSP95] 29	12.2	11.9	0.23	4779	1.07	150	2.22	21	0.8	42
[RSP95] 35	10.4[a]	9.9[b]	1.16	5838	0.36	152	2.46	21	1.1	11
[RSP95] 43	11.8[a]	11.1[b]	0.37	4994	0.91	150	0.78	47	0.9	31
[RSP95] 45A	-	10.1[b]	0.97[b]	5960[b]	0.62	145[c]	-	14	1.1	11
[RSP95] 52	12.0	11.6	0.25	4828	1.03	136	0.39	122	0.8	31
[RSP95] 58	10.4	10.2	1.37	5502	0.61	160	0.57	92	1.1	18

Table 1: (Continued)

Object Name	r	i	$L/L_\odot$	$T_{\rm eff}$	$(B-V)_0$	dist	Period	$v \sin i$	M_*	$\tau_{\rm c}$
	[mag]	[mag]		[K]	[mag]	[pc]	[days]	$[\rm km \cdot s^{-1}]$	$[M_\odot]$	$\times 10^5$ [s]
(1)	(2)	(3)	(4)	(5)	(6)	(7)	(8)	(9)	(10)	(11)
[RSP95] 59	11.6	11.3	0.44	4961	0.78	151	1.31	31	0.9	31
[RSP95] 66	10.8	10.6	0.77	5476	0.64	150	3.28	11	1.0	18
[RSP95] 68	10.9	10.6	0.58	4908	0.82	135	0.99	51	1.1	31
[RSP95] 70	10.7	10.6	0.83	5755	0.65	148	4.25	9	1.1	11
[RSP95] 72	10.6	10.5	0.99	5557	0.60	156	1.05	49	1.1	18
[RSP95] 79	9.0[a]	8.6[b]	4.26	6383	0.40	155	0.75	78	1.5	1
[RSP95] 80	10.3	10.1	1.27	4980	0.89	145	7.25	13	1.3	31
[RSP95] 83	10.5	10.5	1.02	5588	0.58	149	1.74	30	1.0	18
[RSP95] 85	9.7	9.7	2.11	6171	0.48	151	1.33	45	1.3	7
[RSP95] 88A	-	11.4[b]	0.25[b]	4350[b]	1.16	145[c]	0.204[b]	255	0.8	65
[RSP95] 89	12.5	12.0	0.19	4510	1.20	146	4.73	9	0.8	42
[RSP95] 92	10.0	9.9	0.65	5740	0.63	145[c]	1.93	16	1.1	11
[RSP95] 95A	12.3	11.1	0.55	5071	0.83	153	1.22	14	0.9	31

Reference of parameters. (2)(3) r- mag and i- mag: UCAC4 Catalogue (Zacharias et al. 2013), [a]ATLAS All-Sky Stellar Reference Catalogue (Tonry et al. 2018) and [b]Marsden et al. (2009). (4)(5) Luminosity and $T_{\rm eff}$: *Gaia* DR2 (Gaia Collaboration 2018) and [b]Marsden et al. (2009). (6) $(B-V)_0$: Marsden et al. (2009). (7) Distance: *Gaia* DR2 (Bailer-Jones et al. 2018) and [c]van Leeuwen (2007). (8) Period: [b]Patten & Simon (1996) and [b]Barnes et al. (1999). (9) $v \sin i$: Marsden et al. (2009). (10) Canuto & Mazzitelli [CM] Alexander model (D'Antona & Mazzitelli 1994). (11) Landin (2010) model and Noyes et al. (1984) model

3 Results

Figures 2 and 3 show the Hα, Ni I, and Mg I line spectra of the ZAMS stars after subtracting the photospheric absorption. Before subtracting the photospheric absorption component, the Mg I emission component is typically buried by the photospheric absorption, 11 ZAMS stars show Hα as an emission line, and all ZAMS stars show the Ni I line as an absorption component. After the subtraction, the Mg I line is detected as an emission line in 45 ZAMS stars. The Mg I lines of these ZAMS stars show narrow emission, indicative of a chromospheric origin. Their EQWs range from $0.02\,\text{Å}$ to $0.52\,\text{Å}$. A total of 44 ZAMS stars show the Hα emission line. The Ni I line does not present any emission component. The EQWs of the Mg I and Hα emission lines and the FWHMs of the Mg I, Hα, and Ca II IRT emission lines are listed in Table 2.

Some of the chromospheric emission lines detected during a total solar eclipse (Dunn et al. 1968) are also detected in the ZAMS spectra after the subtraction of the absorption components in the order of $64-67$ and $84-87$, P12($\lambda 8750\,\text{Å}$), P14($\lambda 8598\,\text{Å}$), He I ($\lambda 6678\,\text{Å}$), O I ($\lambda 8446\,\text{Å}$), Mg I ($\lambda 8736\,\text{Å}$), Si I ($\lambda 6721, 8557, 8648, 8728, 8742, 8752\,\text{Å}$), Ca I ($\lambda 6573\,\text{Å}$), and Fe I ($\lambda 6518, 6575, 6634, 6713, 6753, 8680, 8686, 8713, 8790, 8824\,\text{Å}$). Among them, P12, P14, He I ($\lambda 6678\,\text{Å}$), and O I ($\lambda 8446\,\text{Å}$) were also detected in the T Tauri star spectra obtained by Hamann & Persson (1992).

The emission line of Mg I at $\lambda 8807\,\text{Å}$ is the most frequently detected lines in the ZAMS spectra. The 45 ZAMS stars out of 47 show the emission lines of Mg I at $\lambda 8807\,\text{Å}$. The second most frequently detected line is the Mg I at $\lambda 8736\,\text{Å}$, which is detected in 40 ZAMS stars. However, this line blends with nearby Si I emission lines ($\lambda 8728, 8742\,\text{Å}$). The Fe I ($\lambda 8689, 8790\,\text{Å}$) and Si I ($\lambda 8728\,\text{Å}$) are detected in the 35 ZAMS stars, the 37 ZAMS stars, and the 30 ZAMS stars, respectively. Other chromospheric emission lines are detected in less numbers of the ZAMS stars, or blended with nearby chromospheric emission lines or OH airgrow. We thus concentrate the following discussion on the Mg I at $\lambda 8807\,\text{Å}$ and Hα lines.

4 Discussion

4.1 Mg I emission line

The line width of the Mg I emission line as a function of those of the Ca II IRT emission lines is plotted in Figure 4. We referred the measured line widths of six T Tauri stars from Hamann & Persson (1992). These T Tauri stars show several prominent emission lines of Mg I and Mg II, which are considered to be formed in the chromosphere or the transition region.

The Mg I line width shows a positive correlation with each Ca II IRT line width. The Mg I

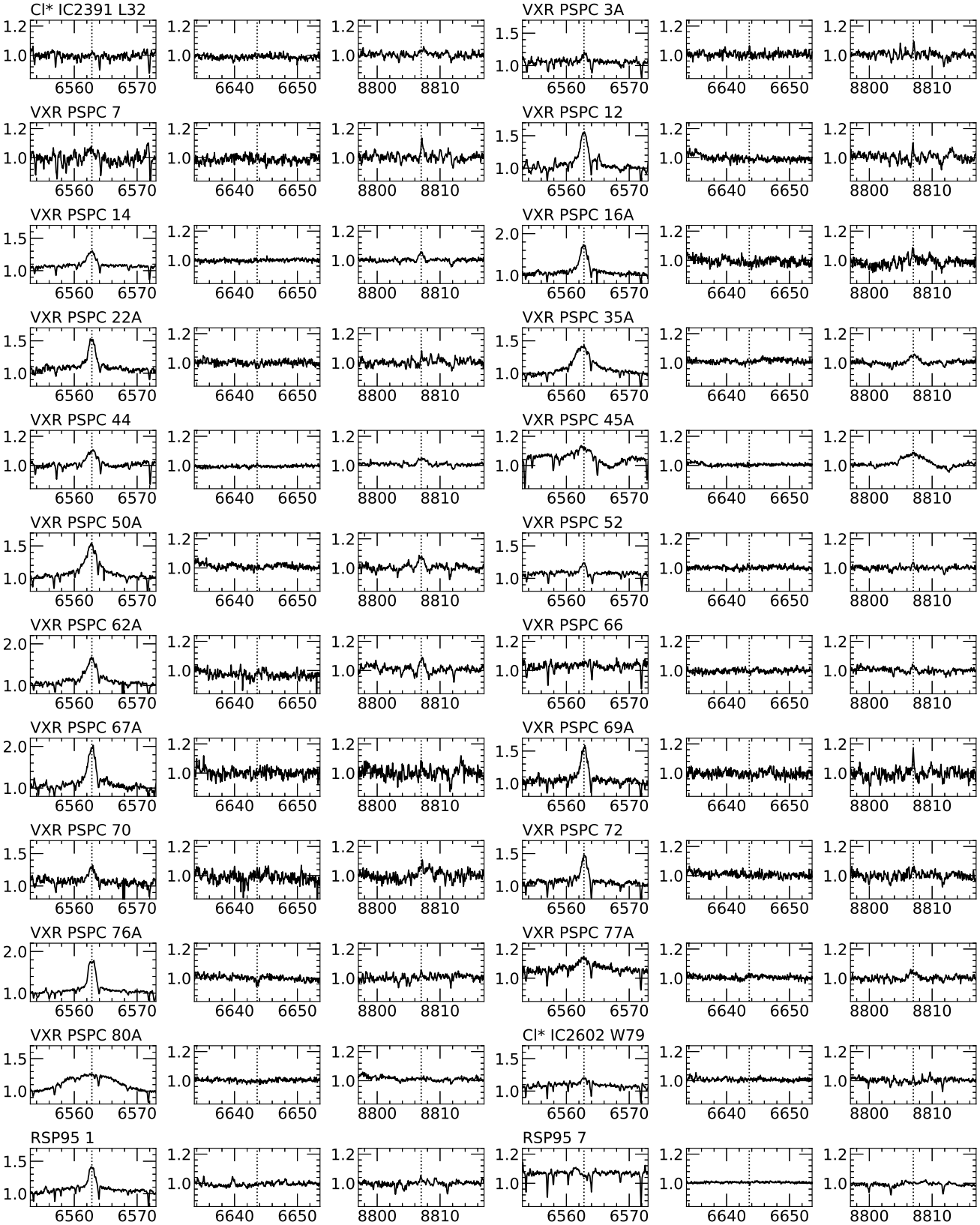

Fig. 2: Hα (6563 Å), Ni I (6644 Å), and Mg I (λ8807 Å) emission lines of ZAMS stars belonging to IC 2391 and IC 2602. Continuum is normalized to unity. Photospheric absorption lines are already subtracted.

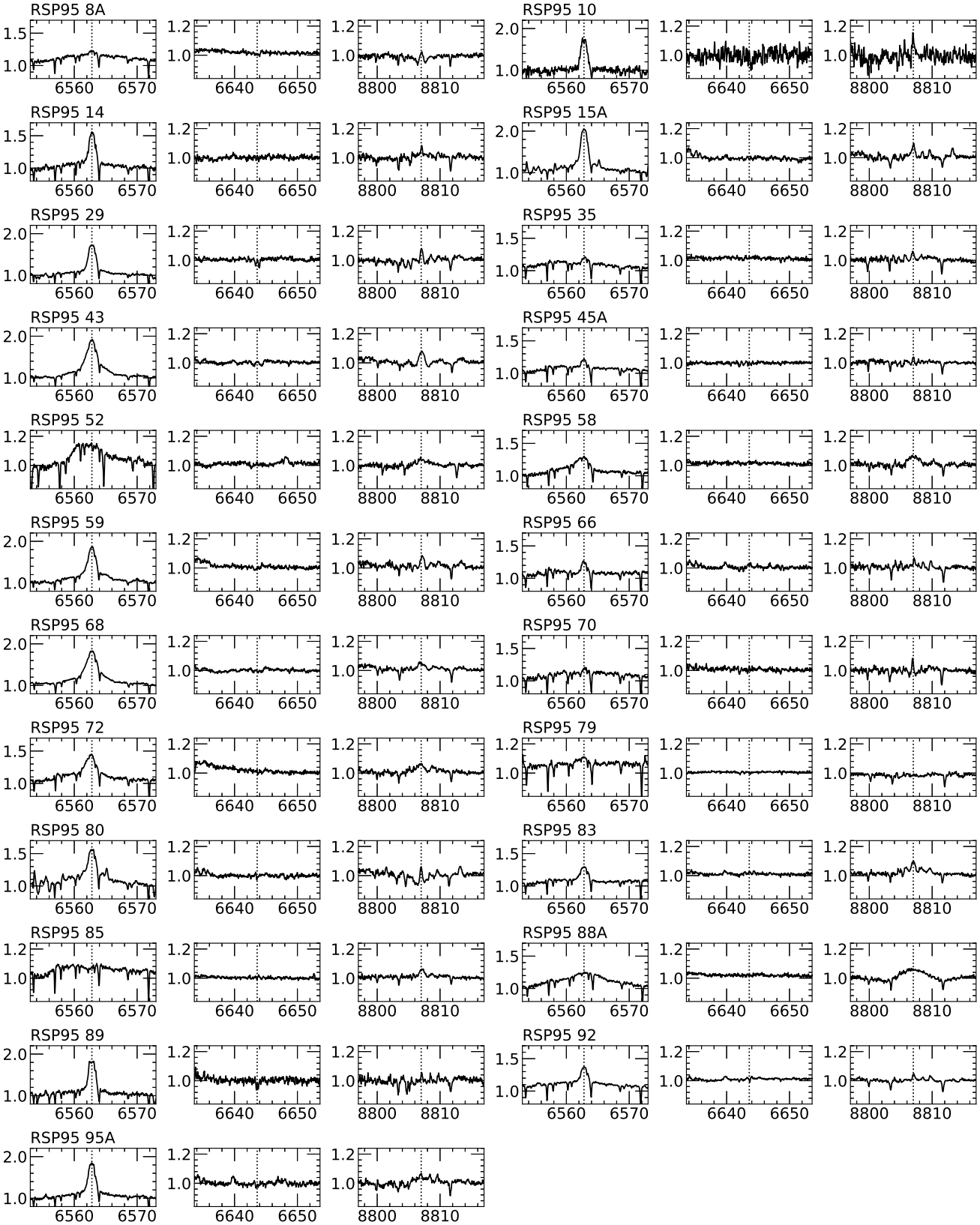

Fig. 3: Hα (6563 Å), Ni I (6644 Å), and Mg I (λ8807 Å) emission lines of ZAMS stars belonging to IC 2602. Continuum is normalized to unity. Photospheric absorption lines are already subtracted.

emission lines in most ZAMS spectra are narrower than the Ca II IRT lines. This is consistent with Hamann & Persson (1992), who claimed that these differences in the widths might be attributed to the different depths of the line formations, where the velocity fields are different. Based on the non-LTE solar model derived by Vernazza et al. (1981), the emission components of the Ca II IRT lines are formed $700 - -1200\,\mathrm{km}$ above the photosphere. Fleck et al. (1994) suggested that the Mg I emission line is formed in the chromosphere, $500\,\mathrm{km}$ above the photosphere.

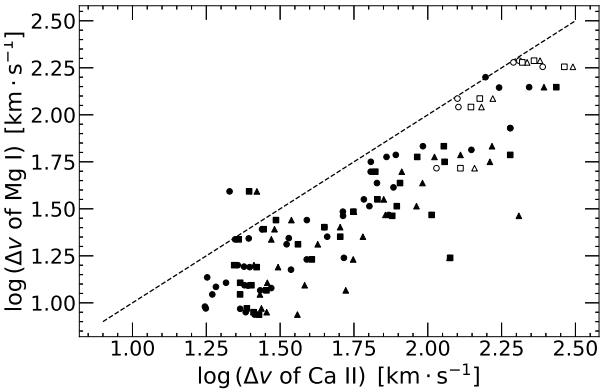

Fig. 4: Relationships between line widths $\Delta\nu$ of Ca II IRT emission lines and line width of Mg I emission line ($\lambda 8807\,\mathrm{Å}$). Filled symbols represent ZAMS stars in this study and open symbols represent T Tauri stars cited in Hamann & Persson (1992). Circles, triangles, and squares symbols show Ca II IRT emission lines ($\lambda 8498, 8542, 8662\,\mathrm{Å}$), respectively. Dashed line represents $\Delta\nu\,\mathrm{of\,Ca\,II} = \Delta\nu\,\mathrm{of\,Mg\,I}$.

Subsequently, we investigated the intensity of the Mg I emission line. To eliminate the dependence of the surface flux on the $T_{\rm eff}$ of the objects, we converted the EQW of the Mg I emission line into the ratio of the surface flux of the emission line to the stellar bolometric luminosity, $R'_{\rm Mg\,I}$. This $R'_{\rm Mg\,I}$ is similar to the parameter, $R'_{\rm HK}$, derived from the Ca II H and K lines, as described by Noyes et al. (1984). In addition to Ca II H and K emission lines, $R'_{\lambda 8542}$, the ratio of the surface flux of the Ca II $\lambda 8542\,\mathrm{Å}$ line to the stellar bolometric luminosity, was previously used by Soderblom et al. (1993) and James & Jeffries (1997). $R'_{\lambda 8498}, R'_{\lambda 8542}$, and $R'_{\lambda 8662}$ were used for the Ca II IRT emission lines by Marsden et al. (2009) and Yamashita et al. (2020). R' was used as a measure of the strengths of chromospheric emission lines, and its dependence on $N_{\rm R}$ has been examined. We first calculated the continuum flux per unit area at a stellar surface, F, as

$$\log \frac{f}{f_0} = -\frac{2}{5} \times m_{i*}, \tag{1}$$

$$F = f \times \left(\frac{d}{R_*}\right)^2, \tag{2}$$

where f is the i-band continuum flux of the object per unit area as observed on the Earth. m_{i*} is the apparent magnitude of the object in the i-band. The i-band continuum flux per unit area under $m_i =$

$0\,\mathrm{mag}$ (the AB system) condition, f_0, is $1.852 \times 10^{-12}\,\mathrm{W \cdot m^{-2} \cdot \AA^{-1}}$ (Fukugita et al. 1996). d denotes the distance of an object from the Earth. R_* is the stellar radius estimated using the Stefan–Boltzmann law with the photospheric luminosity and $T_{\rm eff}$ of the objects. Subsequently, F was multiplied by the EQW of the Mg I emission line and converted into the surface flux, F',

$$F' = F \times \mathrm{EQW}. \tag{3}$$

Using $T_{\rm eff}$ of the target star, $R'_{\rm Mg\,I}$ is calculated as

$$R'_{\rm Mg\,I} = \frac{F'}{\sigma T_{\rm eff}^4}, \tag{4}$$

where σ is the Stefan–Boltzmann constant. The $R'_{\rm Mg\,I}$ values for the ZAMS stars are listed in Table 2. We also referred EQW of an Ca II IRT emission line ($\lambda 8542\,\mathrm{\AA}$) from Marsden et al. (2009) and converted it into the ratio of the surface flux of the emission line to the stellar bolometric luminosity, $R'_{\lambda 8542}$, using Eq (3) and Eq (4).

Noyes et al. (1984) and many authors used $N_{\rm R}$ as an indicator of stellar dynamo activity.

$$N_{\rm R} \equiv \frac{P}{\tau_{\rm c}} = \frac{2\pi R_*}{\tau_{\rm c} v \sin i} \langle \sin i \rangle. \tag{5}$$

We used P for 42 ZAMS stars and $v \sin i$ for 5 ZAMS stars from Marsden et al. (2009). Following the method of Marsden et al. (2009), we assumed the random inclinations and multiplied the average value, $\langle \sin i \rangle = 0.785$, in Eq (5). We estimated the $\tau_{\rm c}$ values of the ZAMS stars using the $\tau_{\rm c}$ models for the stars with the age of $50\,\mathrm{Myr}$ (IC 2391) and $30\,\mathrm{Myr}$ (IC 2602) presented in Landin (2010). We fitted $\log \tau_{\rm c}$ as a third-order polynomial function of $\log T_{\rm eff}$. The $\tau_{\rm c}$ model is valid for objects with $T_{\rm eff} < 6810\,\mathrm{K}$. For six ZAMS stars with $T_{\rm eff} > 6180\,\mathrm{K}$ (Cl* IC2391 L32, VXR PSPC 07, VXR PSPC 44, VXR PSPC 66, RSP95 7, and RSP95 79), we applied the approximation of $\tau_{\rm c}$ of Noyes et al. (1984), where $(B-V)_0$ is referred from Marsden et al. (2009).

The relationship between the ratio of the surface flux of the Mg I emission line to the stellar bolometric luminosity, $R'_{\rm Mg\,I}$ and $N_{\rm R}$ of the ZAMS stars is shown in Figure 5. The $R'_{\lambda 8542}$ values of the same ZAMS stars are also shown in the figure. When $N_{\rm R} > 10^{-1.1}$, $R'_{\lambda 8542}$ increases with decreasing $N_{\rm R}$ until it saturates. When $N_{\rm R} < 10^{-1.1}$, $R'_{\lambda 8542}$ reaches a constant level. Based on the discussion by Marsden et al. (2009), chromospheric saturation is suggested for the objects with $N_{\rm R} < 10^{-1.1}$.

In contrast, $R'_{\rm Mg\,I}$ increases with decreasing $N_{\rm R}$ even for the ZAMS stars with $N_{\rm R} < 10^{-1.1}$. The Mg I line is still unsaturated in the saturated regime for the Ca II IRT emission lines. The correlation coefficient between $R'_{\rm Mg\,I}$ and $N_{\rm R}$ for the ZAMS stars showing $\sigma_{\rm Ni\,I}/\sigma_{\rm cont} < 1.2$ is -0.70. The derived linear fit is

$$\log R'_{\rm Mg\,I} = -0.3918 \log N_{\rm R} - 5.532. \tag{6}$$

The correlation is valid even if other $\tau_{\rm c}$ models (Noyes et al. 1984, Kim & Demarque 1996, and Gunn et al. 1998) are used. The Mg I emission line is considered to be a good indicator of chromospheric activity, particularly of active objects.

VXR 45A and [RSP95] 88A show the largest $R'_{\rm Mg\,I}$. Both are fast rotators; $v \sin i$ of VXR 45A and [RSP95] 88A are $235\,{\rm km \cdot s^{-1}}$ and $255\,{\rm km \cdot s^{-1}}$, respectively. FWHMs of the Mg I emission component correspond to $222\,{\rm km \cdot s^{-1}}$ and $159\,{\rm km \cdot s^{-1}}$. Both are comparable to the rotational velocity. It is known that the emission line is significantly broad if the line is formed by accretion (Yamashita et al. 2020). Thus, we consider that the Mg I emission line is broad for these two stars because of their fast rotation. The two ZAMS stars also show broad emission components of Si I ($\lambda 8728\,{\rm \AA}$), but they are blended with other chromospheric emission lines.

Four objects located at Rossby number greater than -0.5 seem outliers, namely Cl* IC2391 L32, VXR PSPC 07, VXR PSPC 44, and VXR PSPC 66. This misalignment may be attributed to the difference of the applied $\tau_{\rm c}$ models. For the objects with $T_{\rm eff} \leq 6180\,{\rm K}$, we applied $\tau_{\rm c}$ model of Landin (2010). However, the four outliers have $T_{\rm eff} > 6180\,{\rm K}$. $T_{\rm eff}$ higher than $6180\,{\rm K}$ is out of range of the model. Instead, we applied the approximation of $\tau_{\rm c}$ of Noyes et al. (1984) for such high temperature objects. We constructed the relationship between $\tau_{\rm c}$ of Landin's model and $\tau_{\rm c}$ of Noyes' approximation for the ZAMS stars with $T_{\rm eff} \leq 6180\,{\rm K}$. The relationship is fitted by a linear function. We estimated the modified $\tau_{\rm c}$ for the four objects by extrapolating the linear function. The modified $\tau_{\rm c}$ is about $10^5\,{\rm s}$ smaller than $\tau_{\rm c}$ estimated with Noyes' approximation, decresing 0.4 in $\log N_{\rm R}$. As a result, the misalighment seems insignificant.

Marsden et al. (2009) argued that chromospheric saturation is caused by a similar mechanism to coronal saturation. Stepien et al. (2001) suggested that coronal saturation is a result of the coronal-emitting regions of a star being filled. Marsden et al. (2009) claimed that the emitting regions of Ca II of the ZAMS stars in $N_{\rm R} < 10^{-1.1}$ completely cover the chromosphere. The unsaturation of the Mg I emission line suggests that the area of its emitting region may be smaller than the Ca II emitting region area.

The theoretical arguments on saturation are still being debated. The linear mean-field dynamo theory suggests that a small $N_{\rm R}$ allows exciting dynamo activity and leads to a strong magnetic strength. Therefore, the strengths of the Ca II emission lines should increase with decreasing $N_{\rm R}$. However, numerous observations evidence that the Ca II emission lines saturate with small $N_{\rm R}$. Schrinner (2013) explained the mechanism of the saturation based on Ohmic dissipation. They suggested that the ratio of the Ohmic dissipation rate to the power generated by the buoyancy increases with decreasing $N_{\rm R}$ for $10^{-2} < N_{\rm R} < 10^{-1}$. The ratio reaches maximum 0.8 for $10^{-3} < N_{\rm R} < 10^{-2}$, and it is independent of the rotation. This implies that the dynamo activity is constant for a small-$N_{\rm R}$

object.

Many other absorption lines have been shown to also exhibit some filling in with chromospheric activity. Thompson et al. (2017) investigated in the difference between high- and low-activity spectra of α Cen B. For the 48 nights, they generated 'relative' spectra by dividing each of the spectra by their lowest-activity spectra and obtained a large number of narrow emission lines such as Fe I $\lambda 4375, 4427, 4462\,\text{Å}$, Ti II $\lambda 4443.81\,\text{Å}$, and V I $\lambda 4444.21\,\text{Å}$. These features most likely originate from plage, spots or a combination of both.

It is probable that the intensity of the Mg I emission line has a positive correlation with the magnetic field strength. Folsom et al. (2016) observed the Zeeman broadening of rapidly rotating G and K dwarfs, whose $N_{\rm R}$ was between 10^{-2} and 10^{0}. It was showed that the large-scale magnetic field strength increases with decreasing $N_{\rm R}$. The magnetic field strength did not saturate with any Rossby number. Chang et al. (1991) confirmed that the Mg I emission lines at $7\,\mu\text{m}$ and $12\,\mu\text{m}$ provide sensitive measures of the magnetic and electric field strengths of the solar atmosphere. The relation between the magnetic field strength and the Mg I emission line at $\lambda 8807\,\text{Å}$ needs to be investigated.

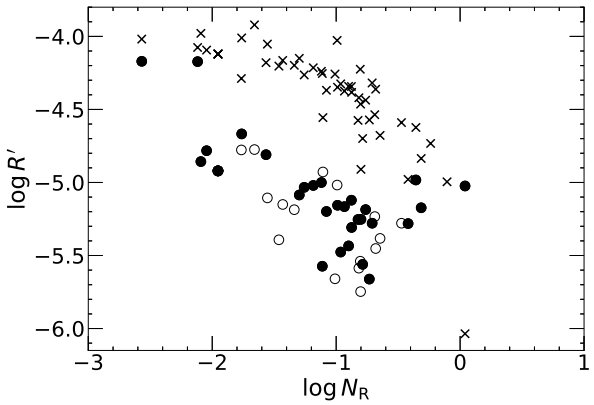

Fig. 5: Relationship between ratio of surface flux of Mg I emission line ($\lambda 8807\,\text{Å}$) to stellar bolometric luminosity $R'_{\rm Mg\,I}$ and Rossby number $N_{\rm R}$ of ZAMS stars (circles). Filled circles represent objects having $\sigma_{\rm Ni\,I}/\sigma_{\rm cont} < 1.2$. Open circles denote objects having $\sigma_{\rm Ni\,I}/\sigma_{\rm cont} \geq 1.2$. Cross symbols represent $R'_{\lambda 8542}$, which is ratio of surface flux of Ca II $\lambda 8542\,\text{Å}$ line to stellar bolometric luminosity, of ZAMS stars.

4.2 Hα emission line

We converted the EQW of the Hα emission line into the ratio of the surface flux of the Hα emission line to the stellar bolometric luminosity, $R'_{\rm H\alpha}$. We first calculated F using Eq (2) and Eq (7).

$$\log \frac{f}{f_0} = -\frac{2}{5} \times m_{r*}, \tag{7}$$

where m_{r*} is the apparent magnitude of the object in the r-band. The r-band continuum flux per unit

area under $m_r = 0\,\mathrm{mag}$ (the AB system) condition, f_0, was $2.780 \times 10^{-12}\,\mathrm{W \cdot m^{-2} \cdot \AA^{-1}}$ (Fukugita et al. 1996). Subsequently, F was multiplied by the EQW of the Hα emission line and converted into F' using Eq (3). By substituting $T_{\rm eff}$ and F' of the target star into Eq (4), $R'_{\rm H\alpha}$ were calculated. The $R'_{\rm H\alpha}$ values for the ZAMS stars are listed in Table 2.

The relationship between $R'_{\rm H\alpha}$ and $N_{\rm R}$ of the ZAMS stars is shown in Figure 6. We also plot R' of the Ca II IRT emission line at $\lambda 8542\,\mathrm{\AA}$ referred from Marsden et al. (2009). The ZAMS stars tend to show larger $R'_{\rm H\alpha}$ as $N_{\rm R}$ becomes smaller. In contrast, the ZAMS stars with $N_{\rm R} < 10^{-1.1}$ have $R'_{\rm H\alpha} \sim 10^{-3.9\pm0.5}$. This is the same as the results the Ca II IRT emission lines. However, the scatter of $R'_{\rm H\alpha}$ seems larger than that of $R'_{\lambda 8542}$. It is likely that the extra scatter is due to the more strongly non-LTE nature of the Hα source function (Cram & Mullan 1979) and its strange optical depth behavior in cooler stars (Houdebine et al. 1995).

Newton et al. (2017) investigated the relationship between $N_{\rm R}$ and $L_{\rm H\alpha}/L_{\rm bol}$, the H$\alpha$ emission line to stellar bolometric luminosity ratio for M dwarfs. The M dwarfs having small $N_{\rm R}$ showed larger $L_{\rm H\alpha}/L_{\rm bol}$ in $N_{\rm R} \geq 10^{-0.67}$. When $N_{\rm R} \leq 10^{-0.67}$, $L_{\rm H\alpha}/L_{\rm bol}$ reached a constant level at 1.85×10^{-4}.

Frasca et al. (2017) observed the Hα, He I, Na I, and Ca II IRT lines of young stellar objects (YSOs) in the Lupus star forming region. One object did not show Hα emission line; however, it was proved that the photospheric absorption component was filled with the chromospheric emission. Most of the young stellar objects show chromospheric emission lines with $R'_{\rm H\alpha} \leq 10^{-3.7}$. The ZAMS stars in our targets also show $R'_{\rm H\alpha} \leq 10^{-3.7}$. Before subtracting the absorption component, a portion of the objects showing featureless spectra at Hα may indeed be chromospherically active stars.

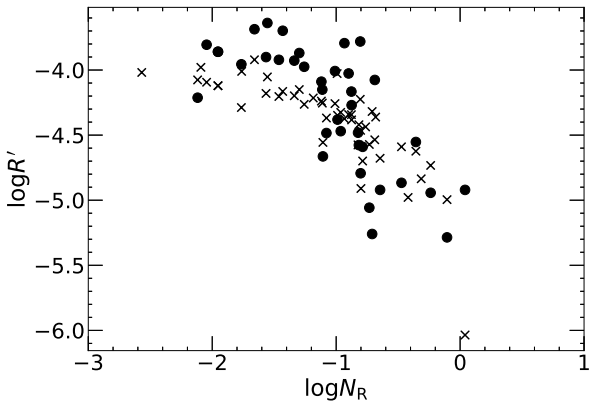

Fig. 6: Relationship between ratio of surface flux of Hα emission line ($\lambda 6563\,\mathrm{\AA}$) to stellar bolometric luminosity $R'_{\rm H\alpha}$ and Rossby number $N_{\rm R}$ of ZAMS stars (filled circles). Cross symbols represent $R'_{\lambda 8542}$, which is ratio of surface flux of Ca II $\lambda 8542\,\mathrm{\AA}$ line to stellar bolometric luminosity, of ZAMS stars.

5 Conclusion

We investigated the infrared Mg I emission lines ($\lambda 8807\,\text{Å}$) of 47 ZAMS stars belonging to IC 2391 and IC 2602. Archived data obtained using the AAT and the UCLES were used. After subtracting the spectra of the inactive stars from the ZAMS spectra, Hα, Ca II, and Mg I were detected as the emission lines.

1. The infrared Mg I emission line width shows a positive correlation with each Ca II IRT line width. Most of the ZAMS stars show the narrower Mg I emission lines, instead of the Ca II IRT emission lines. The Mg I emission lines are detected from the most of the ZAMS stars. After subtracting the photospheric absorption components, the ZAMS stars with smaller Rossby numbers show stronger Mg I emission lines. The Mg I line is unsaturated even in "the saturated regime for the Ca II emission lines," i.e., $N_{\rm R} < 10^{-1.1}$. The Mg I emission line is considered to be a good indicator of chromospheric activity, particularly for active objects.
2. The strength of the Hα emission line is as strong as those of young stellar objects showing chromospheric emission lines.

Acknowledgments

This study is based on the data acquired using the Anglo-Australian Telescope. We acknowledge the traditional custodians of the land on which the AAT stands, the Gamilaraay people, and pay our respects to the elders past and present. This research is also based on the observations made with the ESO Telescopes at the La Silla Paranal Observatory under programs ID 71.B-0529(A), 073.B-0607(A), 076.B-0055(A), 084.D-0965(A), 086.D-0062(A), 087.D-0010(A), 099.D-0410(A), and 266.D-5655(A). M. Y. was supported by a scholarship from the Japan Association of University Women, and would like to thank them. Y. I. is supported by JSPS KAKENHI grant number 17K05390.

References

Bailer-Jones, C. A. L., Rybizki, J., Fouesneau, M., Mantelet, G., & Andrae, R. 2018, ApJ., 156, 58

Baliunas, S., Sokoloff, D., & Soon, W. 1996, ApJ., 457, L99

Barnes, S. A., Sofia, S., Prosser, C. F., & Stauffer, J. R. 1999, ApJ, 516, 263

Barrado y Navascues, D., Stauffer, J. R., & Jayawardhana, R. 2004, ApJ, 614, 386

Brun, A. S., & Browning, M. K. 2017, Living Rev Sol Phys, 14

Chang, E. S., Avrett, E. H., Noyes, R. W., Loeser, R., & Mauas, P. J. 1991, ApJ, 379, L79

Cram, L. E., & Mullan, D. J. 1979, ApJ, 234, 579

D'Antona, F., & Mazzitelli, I. 1994, ApJS, 90, 467

D'Orazi, V., & Randich, S. 2009, A&A, 501, 553

Dunn, R. B., Evans, J. W., Jefferies, J. T., et al. 1968, ApJS, 15, 275

Feinstein, A. D., Montet, B. T., Foreman-Mackey, D., et al. 2019, PASP, 131

Fleck, B., Deubner, F.-L., Maier, D., & Schmidt, W. 1994, IAU Symp, 154, 65

Folsom, C. P., Petit, P., Bouvier, J., et al. 2016, MNRAS, 457, 580

Frasca, A., Biazzo, K., Alcala, J. M., et al. 2017, A&A, 602, 1

Fukugita, M., Ichikawa, T., Gunn, J. E., et al. 1996, AJ, 111, 1748

Furmeister, Schmitt, and Hauschildt (2005)

Gaia Collaboration, 2018, A&A, 616, A1

Gallet, F., & Bouvier, J. 2015, A&A, 577, 1

Gunn, A. G., Mitrou, C. K., & Doyle, J. G. 1998, MNRAS, 296, 150

Gutierrez Albarran, M. L., Montes, D., M. Gomez Garrido., et al. 2020, A&A, A71, 1

Hamann, F., & Persson, S. E. 1992a, ApJ Suppl., 82, 247

Houdebine, E. R., Doyle, J. G., & Koscielecki, M. 1995, A&A, 294, 773

James, D. J., & Jeffries, R. D. 1997, Mon. Notices Royal Astron. Soc., 291, 252

Jung, Y. K., & Kim, Y.-C. 2007, J. Astron. Space Sci., 24, 1

Kim, Y. C., & Demarque, P. 1996, AJ, 457, 340

Landin, N. R., Mendes, L. T. S., & Vaz, L. P. R. 2010, Astron Astrophys, 510, 1

Linsky, J. L., Hunten, D. M., Sowell, R., 1979, ApJS, 41, 481

Marsden, S. C., Carter, B. D., & Donati, J.-F. 2009, MNRAS, 399, 888

Neuhauser, R., Strerzik, M. F., Schmitt, J. H. M. M., Wichmann, R., & Krautter, J. 1995, A&A, 297, 391

Newton, E. R., Irwin, J., Charbonneau, D., et al. 2017, Astrophys J, 834, 85

Nordstrom, B., Andersen, J., Holmberg, J., et al. 2004, Publ. Astron. Soc. Aust., 21, 129

Noyes, R. W., Hamann, F. W., Baliunas, S. L., & Vaughan, A. H. 1984, AJ, 279, 763

Parker, E. N. 1955, ApJ, 122, 293

Patten, B. M., & Simon, T. 1996, ApJ Suppl., 106, 489

Randich, S., Schmitt, J. H. M. M., Prosser, C. F., & Stauffer, J. R. 1995, A&A, 300, 134

Randich, S., Pallavincini, R., Meola, G., Stauffer, J. R., & Balachandran, S. 2001, A&A, 372, 862

Scargle, J. D. 1982, AJ, 263, 835

Schrinner, M. 2013, MNRAS, 431, 78

Skumanich, A. 1972, ApJ, 171, 565

Soderblom, D. R., Stauffer, J. R., & Hudon, J. D. 1993, ApJ, 85, 315

Soubiran, C., Cantat-Gaudin, T., Romero-Gomez, M., et al. 2018, A&A, 619, A155

Stauffer, J. R., Hartmann, L. W., Prosser, C. F., et al. 1997, ApJ, 479, 776

Stepien, K., Schmitt, J. H. M. M., & Voges, W. 2001, A&A, 370, 157

Thompson, A. P. G., Watson, C. A., Mooij, E. J. W., & Jess, D. B. 2017, MNRAS, 468, L16

Tonry, J. L., Denneau, L., Flewelling, H., et al. 2018, ApJ, 867, 105

van Leeuwen, F. 2007, A&A, 474, 653

Vernazza, J. E., Avrett, E. H., & Loeser, R. 1973, ApJ, 184, 605

Vernazza, J. E., Avrett, E. H., & Loeser, R. 1981, ApJS, 45, 635

Yee, S. W., Petigura, E. A., & von Braun, K. 2017, ApJ, 836, 77

Yamashita, M., Itoh, Y., & Takagi, Y. 2020, PASJ, 72, 80

Zacharias, N., Finch, C. T., Girard, T. M., et al. 2013, ApJ, 145, 1

Table 2: EQWs, FWHMs, and R' of ZAMS stars belonging to IC 2391 and IC 2602.

Object name	EQW [Å]		FWHM $[\mathrm{km \cdot s^{-1}}]$					$\frac{\sigma_{\mathrm{Ni\,I}}}{\sigma_{\mathrm{cont}}}$	$\log N_{\mathrm{R}}$	$\log R'$	
	Mg I	Hα	Mg I	Hα	Ca II	Ca II	Ca II			Mg I	Hα
	λ8807	λ6563	λ8807	λ6563	λ8498	λ8542	λ8662			λ8807	λ6563
IC 2391											
Cl* IC2391 L32	0.08 ± 0.07	$< 0.41^{\dagger}$	61	-	78	129	76	0.88	-0.31	-5.17	-
VXR PSPC 3A	0.05 ± 0.02	0.10 ± 0.05	9	38	18	27	17	1.22	-0.65	-5.38	-4.92
VXR PSPC 7	0.10 ± 0.03	0.10 ± 0.07	17	81	52	118	51	0.90	0.04	-5.02	-4.92
VXR PSPC 12	0.04 ± 0.03	0.86 ± 0.09	9	60	24	28	24	0.71	-0.90	-5.43	-4.03
VXR PSPC 14	0.08 ± 0.02	0.34 ± 0.06	31	71	52	56	51	1.08	-0.99	-5.16	-4.38
VXR PSPC 16A	0.10 ± 0.04	0.93 ± 0.13	22	62	34	-	33	0.91	-1.26	-5.03	-3.98
VXR PSPC 22A	0.08 ± 0.03	0.57 ± 0.09	39	58	21	26	21	1.06	-0.88	-5.12	-4.17
VXR PSPC 35A	0.17 ± 0.07	1.53 ± 0.14	65	148	141	-	138	1.04	-2.05	-4.78	-3.81
VXR PSPC 44	0.12 ± 0.04	0.27 ± 0.05	56	79	64	162	63	0.97	-0.36	-4.98	-4.55
VXR PSPC 45A	0.50 ± 0.09	0.55 ± 0.10	140	222	174	-	171	0.92	-2.12	-4.17	-4.21
VXR PSPC 50A	0.16 ± 0.06	1.27 ± 0.12	41	117	77	-	75	1.14	-1.76	-4.67	-
VXR PSPC 52	0.03 ± 0.01	0.21 ± 0.05	13	48	21	29	20	1.05	-0.79	-5.56	-4.59
VXR PSPC 62A	0.18 ± 0.05	1.07 ± 0.16	35	85	61	71	60	1.25	-1.76	-4.78	-3.96
VXR PSPC 66	0.06 ± 0.03	$< 0.39^{\dagger}$	29	-	74	72	72	0.85	-0.42	-5.28	-
VXR PSPC 67A	0.08 ± 0.06	1.65 ± 0.19	25	68	27	30	27	1.19	-0.93	-5.17	-3.79
VXR PSPC 69A	0.09 ± 0.03	0.59 ± 0.09	12	50	30	-	29	0.74	-1.22	-5.00	-4.09
VXR PSPC 70	0.06 ± 0.04	0.28 ± 0.10	28	56	39	35	38	0.59	-0.82	-5.25	-4.48
VXR PSPC 72	0.05 ± 0.03	0.47 ± 0.06	22	52	25	-	24	1.06	-0.88	-5.31	-4.27
VXR PSPC 76A	0.03 ± 0.02	1.60 ± 0.06	14	59	18	-	18	1.96	-0.81	-5.54	-3.78
VXR PSPC 77A	0.13 ± 0.05	0.21 ± 0.04	60	68	72	105	71	1.22	-1.11	-4.93	-4.66
VXR PSPC 80A	0.10 ± 0.10	2.22 ± 0.20	140	362	220	247	216	1.16	-2.09	-4.86	-
IC 2602											
Cl* IC2602 W79	0.02 ± 0.01	0.08 ± 0.02	11	48	19	27	18	0.65	-0.73	-5.66	-5.06
RSP95 1	0.04 ± 0.02	0.34 ± 0.04	12	53	19	-	19	0.94	-0.96	-5.48	-4.47
RSP95 7	$< 0.10^{\dagger}$	0.06 ± 0.02	-	58	-	-	-	1.02	-1.11	-	-5.29
RSP95 8A	0.06 ± 0.02	0.09 ± 0.19	20	582	33	42	33	1.10	-0.76	-5.19	-
RSP95 10	0.07 ± 0.06	0.85 ± 0.17	12	52	25	-	24	1.16	-1.18	-5.02	-
RSP95 14	0.03 ± 0.02	0.60 ± 0.06	9	51	23	-	23	0.71	-1.11	-5.57	-4.15
RSP95 15A	0.07 ± 0.04	1.81 ± 0.05	22	67	22	30	22	1.99	-0.99	-5.02	-
RSP95 29	0.07 ± 0.02	1.09 ± 0.06	15	67	34	-	34	2.51	-1.34	-5.19	-3.93
RSP95 35	0.04 ± 0.02	0.05 ± 0.02	17	41	39	56	38	0.81	-0.71	-5.28	-5.26
RSP95 43	0.13 ± 0.03	2.01 ± 0.07	33	112	63	92	62	1.96	-1.66	-4.77	-3.69
RSP95 45A	0.03 ± 0.01	0.23 ± 0.02	12	42	24	38	23	1.29	-0.68	-5.45	-
RSP95 52	0.13 ± 0.07	1.38 ± 0.10	85	217	190	-	187	1.07	-1.95	-4.92	-3.86
RSP95 58	0.17 ± 0.07	1.07 ± 0.09	68	163	96	165	94	0.97	-1.57	-4.81	-3.90

Table 2: (Continued)

Object name	EQW [Å]		FWHM $[\mathrm{km \cdot s^{-1}}]$					$\frac{\sigma_{\mathrm{NII}}}{\sigma_{\mathrm{cont}}}$	$\log N_{\mathrm{R}}$	$\log R'$	
	Mg I	Hα	Mg I	Hα	Ca II	Ca II	Ca II			Mg I	Hα
	λ8807	λ6563	λ8807	λ6563	λ8498	λ8542	λ8662			λ8807	λ6563
RSP95 59	0.08 ± 0.03	1.95 ± 0.07	22	84	46	60	45	1.35	-1.43	-5.15	-3.70
RSP95 66	0.02 ± 0.01	0.14 ± 0.03	9	41	26	36	25	1.25	-0.80	-5.75	-4.79
RSP95 68	0.08 ± 0.03	2.01 ± 0.06	43	110	67	96	66	1.47	-1.55	-5.11	-3.64
RSP95 70	0.06 ± 0.01	0.11 ± 0.02	12	44	27	53	27	1.64	-0.47	-5.28	-4.87
RSP95 72	0.09 ± 0.04	1.15 ± 0.08	50	111	64	82	63	1.19	-1.30	-5.09	-3.87
RSP95 79	$< 0.09^{\dagger}$	0.10 ± 0.02	-	92	60	-	59	1.10	-0.24	-	-4.94
RSP95 80	0.07 ± 0.02	0.76 ± 0.06	16	77	23	26	22	1.34	-0.69	-5.23	-4.08
RSP95 83	0.08 ± 0.02	0.28 ± 0.03	25	52	45	51	44	1.20	-1.08	-5.20	-4.48
RSP95 85	0.07 ± 0.02	$< 0.20^{\dagger}$	29	-	52	203	51	1.08	-0.80	-5.25	-
RSP95 88A	0.52 ± 0.09	1.56 ± 0.18	159	456	157	-	154	0.78	-2.57	-4.17	-
RSP95 89	0.02 ± 0.02	1.03 ± 0.08	10	56	18	-	17	1.80	-1.01	-5.66	-4.01
RSP95 92	0.03 ± 0.01	0.23 ± 0.02	15	50	25	31	24	1.86	-0.82	-5.59	-4.58
RSP95 95A	0.04 ± 0.02	1.06 ± 0.08	16	62	24	-	23	1.34	-1.46	-5.39	-3.92

$^{\dagger}3\sigma$ upper limit